European Journal of Medicinal Chemistry 265 (2024) 116112

Contents lists available at ScienceDirect

European Journal of Medicinal Chemistry

journal homepage: www.elsevier.com/locate/ejmech

Research paper

Mitochondria-targeted iridium(III) complexes encapsulated in liposome induce cell death through ferroptosis and gasdermin-mediated pyroptosis

Chunxia Huang [a,1], Yuhan Yuan [a,b,1], Gechang Li [a], Shuang Tian [a], Huiyan Hu [a], Jing Chen [a], Lijuan Liang [a], Yi Wang [a], Yunjun Liu [a,*]

[a] School of Pharmacy, Guangdong Pharmaceutical University, Guangzhou, 510006, China
[b] Foshan women and children hospital, Foshan, 528000, China

ARTICLE INFO

Keywords:
Iridium(III) complexes
Apoptosis
Ferroptosis
Pyroptosis
In vivo antitumor
RNA-Sequence

ABSTRACT

This paper unveils a novel perspective on synthesis and characterization of the ligand 5-bromo-2-amino-2'-(phenyl-1H-imidazo[4,5-f][1,10]phenanthroline) (BAPIP), and its iridium(III) complexes $[Ir(PPY^{-})_2(BAPIP)](PF_6)$ (1a, with PPY^{-} as deprotonated 2-phenylpyridine), $[Ir(PIQ^{-})_2(BAPIP)](PF_6)$ (1b, piq^{-} denoting deprotonated 1-phenylisoquinoline), and $[Ir(BZQ^{-})_2(BAPIP)](PF_6)$ (1c, bzq^{-} signifying deprotonated benzo[h]quinoline). Systematic evaluation of the cytotoxicity of 1a, 1b, and 1c across diverse cell lines encompassing B16, HCT116, HepG2, A549, HeLa, and LO2 using 3-(4,5-dimethylthiazol-2-yl)-2,5-diphenyltetrazolium bromide (MTT) method. Unexpectedly, compounds 1b and 1c demonstrated no cytotoxicity against the above cell lines. Motivated by the pursuit of heightened anti-proliferative potential, a strategic encapsulation approach yielded liposomes 1alip, 1blip, and 1clip. As expectation, 1alip, 1blip, and 1clip displayed remarkable anti-proliferative efficacy, particularly noteworthy in A549 cells, exhibiting IC_{50} values of 4.9 ± 1.0, 5.9 ± 0.1, and 7.6 ± 0.2 μM, respectively. Moreover, our investigation illuminated the mitochondrial accumulation of these liposomal entities, 1alip, 1blip, and 1clip, evoking apoptosis through the mitochondrial dysfunction mediated by reactive oxygen species (ROS). The ferroptosis was confirmed by decrease in glutathione (GSH) concentrations, the downregulation of glutathione peroxidase 4 (GPX4), increase of high mobility group protein 1 (HMGB1), and lipid peroxidation. Simultaneously, pyroptosis as another mode of cell death was undertaken. RNA-sequencing was employed to investigate intricate signalling pathways. In vivo examination provided tangible evidence of 1alip in effectively curbing tumor growth. Collectively, this study provides a multifaceted mode of cellular demise orchestrated by 1a, 1alip, 1blip, and 1clip, involving pathways encompassing apoptosis, ferroptosis, and pyroptosis.

1. Introduction

Malignant neoplasms pose a formidable threat to human well-being, engendering a reduction in the quality of life and, at times, culminating in mortality. The challenge of combating cancer is monumental, given its proclivity for recurrence, metastasis, dearth of safe and efficacious therapies, and the annual escalation in morbidity and mortality rates [1]. In the wake of swift advancements in detection methodologies and treatment modalities, immunotherapy, gene therapy, and chemotherapy emerge as valid clinical strategies for a treatment of malignancies [2–4]. Although myriad antineoplastic agents have been used to address their respective malignancies, the multifaceted resistance and systemic toxicities persist as an imposing impediment to effective chemotherapy. Thus, the scientific community's focus pivots towards conceiving novel antineoplastic chemotherapies and negligible side effects [5]. Cisplatin's clinical deployment have been limited by its systemic toxicity, precipitating deleterious adversities such as profound emesis, auditory debilitation, and renal compromise. Consequently, the scientific vanguard embarks on a quest for alternative metal complexes as surrogates for cisplatin [6,7]. Cyclometalated iridium(III) complexes, an intriguing subset of compounds, have attracted considerable attention [8,9]. The cyclometalated complexes constituted by iridium(III) as the nucleus, ensconced between two cyclic ligands and a bidentate ligand, the chemical properties of which can be adjusted by changing the chemical

* Corresponding author.
E-mail address: lyjche@gdpu.edu.cn (Y. Liu).
[1] These authors contribute equally.

https://doi.org/10.1016/j.ejmech.2023.116112
Received 5 November 2023; Received in revised form 25 December 2023; Accepted 29 December 2023
Available online 1 January 2024

structure, which is more diverse than the typical planar structure of platinum complexes [10]. The distinctive attributes encompass an extended phosphorescence lifespan, pronounced photostability, and cellular ingress capability, endowing it with potential not only as an anticancer agent but also as an innovative biological probe [11–18]. Although iridium(III) complexes have strong anticancer effects, many problems remain to be solved, including incomplete metabolism and poor water solubility. Nanosystems are capable of passive targeting the tumor tissue, resulting in the accumulation of nanoparticles near tumor cells and the release of drugs [19–21]. Liposomes, one of the most fascinating organic nanostructures, are synthetic lipid vesicles with a hydrophilic cavity surrounded by an amphiphilic phospholipid bilayer [22]. Hence, liposomes have been intensively investigated as a lipid bilayer structure for their diagnostic and drug-delivery functions [23, 24]. Several studies in recent years have described liposome-loaded iridium complex-based drug delivery systems [25–27]. The iridium (III) complexes encapsulated in polyethylene-glycollated liposomes can be used as cancer therapeutics.

In our previous work, we found that iridium(III) complexes with polypyridyl ligands apip (2-aminophenylimidazo[4,5-f][1,10]phenanthroline), maip (3-aminophenylimidazo[4,5-f][1,10]phenanthroline) and paip (4-aminophenylimidazo[4,5-f][1,10]phenanthroline) containing $–NH_2$ as substitute group show high anticancer effect on A549 and B16 cells [28]. Moreover, we also found that the polypyridyl iridium (III) complex $[Ir(ppy)_2(BBIP)](PF_6)$ (BBIP = 2-(7-bromo-2*H*-benzo[*d*]imidazole-4-yl)-1*H*-imidazo[4,5-*f*][1,10]phenanthroline) with Br atom as substitute group also displays strong ability to inhibit A549 (IC_{50} = 4.9 ± 0.5 μM) and HeLa (IC_{50} = 9.4 ± 0.5 μM) cell proliferation [29]. Additionally, halogen atoms are among the most popular substituents utilized for the optimization of the properties of biologically active compounds, moreover, the halogen atoms can form both hydrophobic and electrostatic interactions with biological targets [30]. The literatures reported that the compounds with Br atom as substitute group reveal high anticancer activity [31–33]. Therefore, based on the above findings and reports, in this article, a new ligand 5-bromo-2-amino-2'-(phenyl-1H-imidazo[4,5-f][1,10]phenanthroline (BAPIP) with $–NH_2$ and Br atom as substitute groups and iridium(III) complexes $[Ir(PPY^-)_2(BAPIP)](PF_6)$ (1a, PPY^- = deprotonated 2-phenylpyridine), $[Ir(PIQ^-)_2(BAPIP)](PF_6)$ (1b, PIQ^- = deprotonated 1-phenylisoquinoline) and $[Ir(BZQ^-)_2(BAPIP)](PF_6)$ (1c, BZQ^- = deprotonated benzo[h]quinoline) were synthesized and characterized. The ligand BAPIP was formed by the replacement of a hydrogen atom at 4-position of apip with a bromide atom, poor solubility makes it tough for 1a, 1b, 1c to enter the cell. Therefore, 1a, 1b and 1c were wrapped into liposomes, which facilitated the passage of the drug through the cell membrane and thus exhibited excellent anticancer efficacy.

2. Results and discussion

2.1. Chemistry

The ligand BAPIP was synthesized through a reaction involving phenanthroline-5,6-dione, 2-amino-4-bromobenzaldehydedione and NH_4Ac in glacial acetic acid (Scheme 1). Subsequently, compounds 1a, 1b, and 1c were prepared by refluxing $[Ir(PPY^-)_2Cl]_2$, $[Ir(PIQ^-)_2Cl]_2$ and $[Ir(BZQ^-)_2Cl]_2$ with BAPIP using methanol and dichloromethane as a mixed solvent. The characterization of 1a, 1b, and 1c involved High-Resolution Mass Spectroscopy (HRMS) and nuclear magnetic resonance (NMR) spectroscopy. In HRMS, the determined molecular weights were consistent with the expected values. Notably, the ^1H NMR spectra revealed signals corresponding to $–NH_2$ resonances at 4.49 ppm for 1a and 4.48 ppm for 1c. Additionally, owing to probably rapid exchange, the peak of the proton bonded to nitrogen in the imidazole ring was not discovered in the ^1H NMR spectra.

The purities of 1a, 1b, and 1c were assessed via high performance liquid chromatography (HPLC) using a mobile phase consisting of methanol and water in ratios of 72:28, 72:28, and 70:30 for 1a, 1b, and 1c, respectively. The purities of 1a, 1b and 1c were determined as 96.56 %, 98.11 %, and 96.85 %, respectively (Fig. S1 and SI).

Furthermore, the encapsulation of 1a, 1b, and 1c within liposomes, denoted as 1alip, 1blip, and 1clip, was achieved through a film dispersion method, resulting in encapsulation efficiency (EE) values of 87.6 %, 88.3 %, and 85.4 %, respectively. These outcomes indicate successful encapsulation of the complexes within the liposomal structures. The prepared 1alip, 1blip, and 1clip exhibited a yellow hue (Fig. S2a and SI). Their particle sizes were determined as 109.1 nm (±2.4), 95.5 nm (±1.9), and 90.7 nm (±1.3), respectively (Fig. S2b and SI). The ζ-potential measurements unveiled surface mean charges of −21.80 mV, −23.68 mV, and −23.93 mV for 1alip, 1blip, and 1clip, respectively (Fig. S2c and SI), confirming the stability of these complexes-loaded

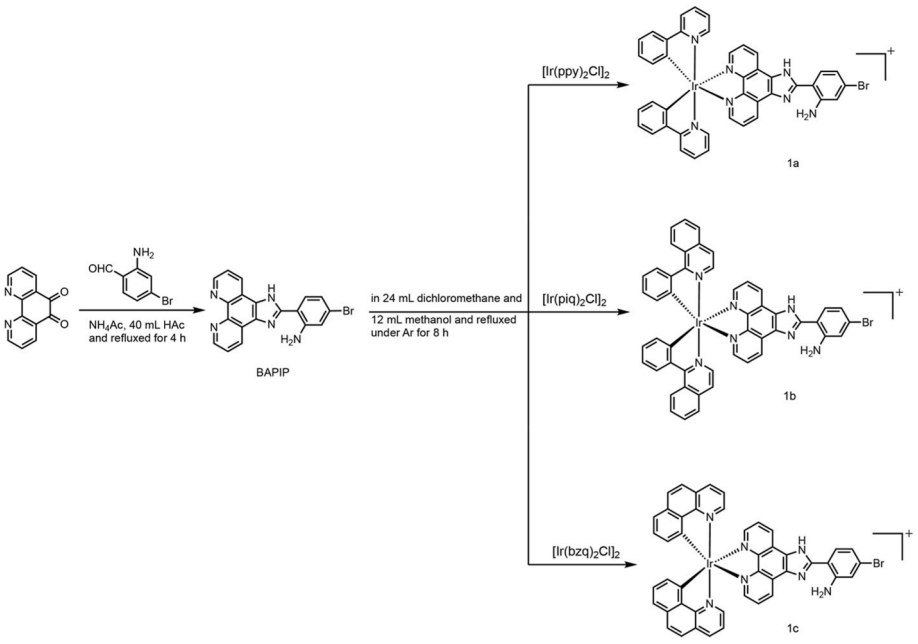

Scheme 1. Synthetic route for ligand BAPIP and complexes 1a, 1b, 1c.

liposomes. Additionally, the stability of 1alip, 1blip and 1clip was examined by UV–Vis spectra, as shown in Fig. S2d (SI), we observed no change in the peak shape at 0 h and 48 h, indicating that the liposome-loaded complexes are stability. The morphology of 1clip was examined by transmission electron microscope (TEM), as seen from Fig. S2e (SI), 1clip displays a spherical particle size.

Subsequently, the release kinetics of 1a, 1b, and 1c from 1alip, 1blip, and 1clip were monitored over 72 h. As illustrated in Fig. S2f (SI), the initial release percentages were observed to be 34.74 % for 1a, 19.94 % for 1b, and 43.87 % for 1c. At 72 h, the release rates increased to 70.14 % for 1a, 41.32 % for 1b, and 88.93 % for 1c. Therefore, the release of 1a, 1b and 1c from 1alip, 1blip and 1clip was carried out slowly.

2.2. Evaluation of cytotoxic activity

The assessment of cytotoxicity for compounds 1a, 1b, 1c, 1alip, 1blip and 1clip was conducted using the 3-(4,5-dimethylthiazol-2-yl)-2,5-diphenyltetrazolium bromide (MTT) method [34]. The cytotoxic efficacy of these compounds on A549, HTC-116, HepG2, B16, HeLa, and non-cancer LO2 cells was quantified in terms of half maximum inhibitory concentration (IC_{50}) values. See from Tables 1 and 1a exhibited a moderate level of cytotoxicity. Intriguingly, compounds 1b and 1c displayed no discernible cytotoxicity. This phenomenon could likely be attributed to the limited solubility of 1b and 1c, impeding their effective cellular internalisation and consequently resulting in the absence of cytotoxic activity for these two compounds. To amplify the intracellular uptaken amounts of 1a, 1b, and 1c, these compounds were encapsulated within liposomal carriers, yielding 1alip, 1blip, and 1clip. Notably, the cytotoxicity of 1alip towards A549 cells was amplified by a factor of 2.94 compared to that of 1a. The IC_{50} values for 1alip, 1blip, and 1clip against A549 cells were determined as 4.9 ± 1.0, 5.9 ± 0.1, and 7.6 ± 0.2 μM, respectively. The anti-proliferative efficacy of 1alip, 1blip, and 1clip surpassed that of cisplatin against B16, HCT116, and HepG2 cells, but lower than liposome entrapped cisplatin (CDDPlip) toward B16 and A549 cells. Their cytotoxicity is comparable with that of liposome-encapsulated $[Ir(bzq^{-})_2(DIPH)](PF_6)$ against HeLa cells (IC_{50} = 6.3 ± 0.2 μM) [27]. Additionally, we also examined the cytotoxic activity of blank liposome against A549 cells, we found that the blank liposomes have no cytotoxic activity toward A549 cells, this is agreement with the results reported in the literature [35]. According to the IC_{50} values, we discovered that 1alip, 1blip and 1clip show the highest anticancer activity towards A549, HeLa and HepG2 cells, respectively, which demonstrates that the liposome-loaded different compounds exhibit different anticancer efficacy toward different cancer cells. This collective evidence substantiates the notion that liposome-encapsulated complexes engender a substantial augmentation in their anticancer potential.

Table 1
IC_{50} values (μM) of 1a, 1b, 1c, 1alip, 1blip, 1clip and liposome-loaded cisplatin (CDDPlip) towards the selected cancer cells for 48 h.

Complex	B16	HCT116	HepG2	A549	HeLa	LO2
1a	16.6 ± 0.2	14.3 ± 0.2	33.8 ± 2.2	14.4 ± 0.5	15.3 ± 3.5	43.8 ± 1.3
1b	>200	>200	>200	>200	>200	>200
1c	>200	>200	>200	>200	>200	>200
1alip	5.7 ± 0.3	6.3 ± 0.1	5.0 ± 0.4	4.9 ± 1.0	6.9 ± 0.2	8.7 ± 1.0
1blip	5.1 ± 0.1	6.2 ± 0.3	9.9 ± 0.2	5.9 ± 0.1	4.4 ± 0.1	7.8 ± 0.2
1clip	8.8 ± 0.4	7.5 ± 0.2	5.9 ± 0.2	7.6 ± 0.2	6.8 ± 0.1	10.3 ± 0.2
cisplatin	18.8 ± 1.2	14.5 ± 2.2	9.1 ± 1.4	6.6 ± 0.7	5.7 ± 1.1	18.3 ± 2.4
CDDPlip	3.6 ± 0.1	nd	nd	1.5 ± 0.1	nd	3.7 ± 1.5

nd: not determination.

2.3. Cellular uptake, co-location, ROS, mitochondrial membrane potential, Ca^{2+} concentration

The requisite for the manifestation of the anticancer activity of complexes resides in their cellular uptake. In this context, an uptaken amount of 1a, 1alip, 1blip, and 1clip by A549 cells was undertaken through laser scanning confocal microscopy. As discerned from Fig. S3a (SI), the treated groups exhibited green fluorescence emanating from the complexes, while the cell nuclei were distinctly stained blue. Upon scrutinizing the merged images, it becomes apparent that 1a, 1alip, 1blip, and 1clip enter the cells and focus on the cytoplasmic locale, while in the 1b, 1c-treated groups, the green fluorescence is the same as that in the control, indicating almost no complexes entering the cells. The results obtained from that cellular uptake are agreement with those of cytotoxic activity.

Given that mitochondria are pivotal in apoptosis, their involvement in the cellular context was explored. Notably, the co-localization of red fluorescence (indicative of mitochondria) and green fluorescence (corresponding to the complex or complex-loaded liposomes) became evident after the entry of 1a, 1alip, 1blip, and 1clip into the cells for 4 h, as depicted in Fig. S3b (SI). This concurrence of signals underscores the convergence of these complexes at the mitochondria.

Mitochondrial dysfunction, a salient hallmark of apoptosis, materializes through the diminution of mitochondrial membrane potential (MMP) and the simultaneous opening of the mitochondrial permeability transition pore (MPTP) [36,37]. To gauge alterations in MMP, the fluorophore JC-1 (5,5′,6,6′-tetrachloro-1,1′,3,3′-tetrethylbenzimidalylcarbocyanine iodide) was harnessed. The transition of JC-1 from a red-fluorescent aggregate to a green-fluorescent monomer within the mitochondria corroborates changes in MMP [38]. Exposure of A549 cells to 1a, 1alip, 1blip, and 1clip for 24 h occasioned a diminution in the red fluorescence (indicative of high MMP) alongside a concomitant elevation in green fluorescence (indicative of low MMP), reflective of a decline in the mitochondrial membrane potential, as presented in Fig. S3c (SI). The quantification of red and green fluorescence is graphically elucidated in Fig. S3d (SI), 0.5 × IC_{50} concentration of 1a, 1alip, 1blip and 1clip show low effect on the change of mitochondrial membrane potential, while A549 cells were treated with 2 × IC_{50} concentration of 1a, 1alip, 1blip and 1clip for 24 h, an obvious change in the ratio of red/green fluorescence was uncovered. These observations further underscore the propensity of 1a, 1alip, 1blip and 1clip to induce a decline in MMP with a concentration-dependent manner.

Concurrent with changes in MMP, the sustained opening of mitochondrial permeability transition pore (MPTP) transpires. This phenomenon is orchestrated by the protein tyrosine phosphatase (PTP), which ensures continuous pore opening when the mitochondrial matrix undergoes elevated osmotic pressure. The outcome encompasses mitochondrial membrane depolarisation and a surge in reactive oxygen species (ROS), ultimately culminating in apoptosis [39,40]. Apparent from Fig. S3e (SI) is the robust green fluorescence in the control and negative groups, indicative of normal MPTP function. Conversely, treatment of A549 cells with 1a, 1alip, 1blip, and 1clip ushered in a substantial reduction in green fluorescence, substantiating their potential to induce continuous MPTP opening.

Given the intertwined relationship between ROS and mitochondrial dysfunction, intracellular ROS content was evaluated using 2,7′-dichlorodihydrofluorescein diacetate (DCFH-DA) as a fluorescence probe. The treatment of A549 cells with 1a, 1alip, 1blip, and 1clip yielded heightened green fluorescence, an effect quantitatively corroborated and presented in Fig. S3f (SI). Notably, the fluorescence intensity in cells treated with 1a exhibited a moderate increment, while 1alip, 1blip, and 1clip induced increments of 2.81, 2.21, and 2.98 times compared to the control, respectively (Fig. 3g and SI). These results collectively underscore the propensity of 1a, 1alip, 1blip, and 1clip to elicit an elevated level of ROS production.

Calcium ions (Ca^{2+}) function as pivotal second messengers

governing diverse cellular processes encompassing gene transcription, cell proliferation, migration, and apoptosis [41]. The elevation in Ca^{2+} level imparts impetus to ROS production, diminishes mitochondrial membrane potential, and triggers sustained MPTP opening, thereby engendering apoptosis [42]. As illustrated in Fig. S3h (SI), the control and 1a-treated groups exhibited modest green fluorescence, whereas in the groups treated with 1alip, 1blip, and 1clip, a marked increase in fluorescence intensity was discovered. Notably, the enhancement was quantified as 2.95, 1.85, and 2.33 times than that of the initial intensity, as illustrated in Fig. S3i (SI). This discernible increase underscores the role of 1a, 1alip, 1blip, and 1clip in eliciting a release of Ca^{2+}, thereby further exacerbating mitochondrial dysfunction and hastening the apoptotic cascade. Based on the above results, we consider that the complexes-loaded liposomes induce apoptosis in A549 cells via a ROS-mediated mitochondrial dysfunction pathway.

2.4. Cell cycle distribution and apoptosis

In eukaryotic organisms, cellular proliferation constitutes a pivotal process underpinning cell growth, development, and tissue regeneration [43]. Therefore, impeding the progression of the cell cycle emerges as a fundamental strategy within the anticancer paradigm, whereby the restraint of cellular proliferation thwarts the advancement of malignancy. As portrayed in Fig. S4a (SI), examining A549 cell populations subjected to 2 × IC_{50} concentration of 1a (IV), 1alip (VII), 1blip (X), and 1clip (XIII) treatments reveals a decline in cell numbers within the G0/G1 and G2/M phases. Correspondingly, a significant increase is observed in the S-phase population, manifesting as a 19.73 % increase for 1a, 26.82 % for 1alip, 23.30 % for 1blip and 22.02 % for 1clip (Table 2). These results substantiate that 1a, 1alip, 1blip, and 1clip effectively suppress cell proliferation during the S-phase with a concentration-dependent manner. Furthermore, it is pertinent to note that 1alip displays a superior capacity in inhibiting cell proliferation compared to its corresponding complex 1a.

The influence of the complexes and their encapsulated liposomes on cellular proliferation inevitably entails an induction of cell death. Within this context, apoptosis emerges as a pivotal mechanism for eliminating senescent cells [44]. As depicted in Fig. S4b (SI), after A549 cells (I) were incubated with 2 × IC_{50} concentration of 1a (IV), 1alip (VII), 1blip (X) and 1clip (XIII) for 24 h, the proportion of cells in early apoptosis (Q3) rises from 1.32 % in the control group to 11.5 % for 1a, 16.8 % for 1alip, 18.3 % for 1blip, and 20.1 % for 1clip-treated groups, respectively (Table 2). These outcomes collectively affirm that 1a, 1alip, 1blip, and 1clip can induce apoptosis with a concentration-dependent manner. Notably, the liposome-encapsulated complex 1alip exhibits an enhanced apoptotic efficacy compared with 1a.

2.5. RNA-sequence, apoptosis-related protein expression

Moving forward, the exploration of RNA sequencing and an assessment of apoptosis-related protein expression were carried out. RNA sequencing stands as an insightful technique capable of unveiling the pathways through which compounds orchestrate cell death. In this regard, an RNA sequencing experiment unveiled the biological processes underpinning the antitumor activity of interest. The heatmap and gene distribution profiles depicted in Fig. 1a and b elucidate that 1alip elicits the downregulation of 367 genes and the upregulation of 534 genes. This cascade of gene expression modulation leads to the enrichment of various cancer-associated signalling pathways as evidenced by the KEGG pathway analysis in Fig. 1c. These pathways encompass TNF, PI3K/AKT, and calcium ion signalling pathways, collectively orchestrating cell apoptosis and demise. The GO enrichment analysis, as illustrated in Fig. 1d, further corroborates the enrichment of biological processes, molecular functions, and cellular components underpinning the observed effects.

A deeper exploration of the apoptotic mechanisms was pursued to corroborate the findings derived from RNA sequencing. The apoptotic cascade is fundamentally directed through two primary pathways: the mitochondrial and death receptor pathways [45]. These pathways depend on the activation of caspases (cysteinyl aspartate-specific proteases), which subsequently cleave numerous proteins, thereby executing apoptosis and culminating in cellular demise, accompanied by distinctive biochemical hallmarks [46]. Caspase 3, operating as an effector caspase, plays a central role in this process, ultimately precipitating cellular death by cleaving death substrates such as poly-ADP ribose polymerase (PARP) [45], and cleaved PARP serves as a functional indicator of apoptosis [47]. In the presented study, the modulation of apoptotic markers including caspases and Bcl-2 family proteins is evident, as depicted in Fig. 1e and **f**. The upregulation of Bax, concurrent with the downregulation of Bcl-2, PI3K, AKT, and caspase 3 expression, is apparent in response to 1a, 1alip, 1blip, and 1clip treatments. The cumulative evidence substantiates that 1a, 1alip, 1blip, and 1clip orchestrate apoptosis by modulating Bcl-2 family protein expression and hindering the PI3K/AKT pathway, a conclusion harmonious with the RNA sequencing analysis.

2.6. Cell ferroptosis studies

Lipid peroxidation is an intricate autoxidation process instigated by the assault of free radicals, contributing significantly to the orchestration of cell demise [48]. Notably, glutathione (GSH) holds a pivotal regulatory role in the facets of cell differentiation, proliferation, and apoptosis [49]. To Illustrating this, Fig. 2a portrays the discernible reduction in GSH levels after a 24-h exposure of A549 cells to 1a, 1alip, 1blip, and 1clip. This observation lucidly underscores the efficacious capability of 1a, 1alip, 1blip, and 1clip to reduce GSH amounts, ultimately culminating in cellular demise. Conversely, in the context of elevated ROS levels, GSH interacts with ROS, resulting in the formation of glutathione disulfide (GSSG). As depicted in Fig. 2b, the diminishment in the GSH/GSSG ratio affirms the reduction in GSH content.

On a parallel note, malondialdehyde (MDA), a product of lipid peroxidation, is serves as an apt gauge of oxidative stress-mediated cellular injury [50]. The depiction in Fig. 2c notably showcases the conspicuous elevation in intracellular MDA content upon treating A549 cells with 1a, 1alip, 1blip, and 1clip. This discernible elevation in MDA content corroborates that 1a, 1alip, 1blip, and 1clip can induce lipid peroxidation.

As a programmed cell death, ferroptosis assumes a significant role characterized by its intricate interplay with lipid peroxidation, facilitated through glutathione peroxidase 4 (GPX4) as the principal pathway [51]. Inactivation of GPX4 results in the accumulation of lipid peroxides, thereby instigating heightened ROS levels [52]. Notably, ferroptosis can be induced by activating high mobility group protein 1 (HMGB1), which functions as both a damage-associated molecule and a nexus between ferroptosis and pyroptosis [53,54]. Fig. 2d shows that 1a, 1alip, 1blip, and 1clip downregulated GPX4 expression in comparison to the control, while concurrently, an augmented expression of HMGB1 is evident

Table 2
The percentage of cell at the S phase and early apoptosis after A549 cells exposed to different concentration (μM) of 1a, 1alip, 1blip and 1clip for 24 h.

	Control	1a			1alip			1blip			1clip		
Concentration		8.3	16.6	33.2	2.85	5.7	11.4	2.55	5.1	10.2	4.4	8.8	17.5
Percentage at S phase (%)	23.29	41.58	42.90	43.12	47.30	48.46	50.21	42.58	44.71	46.69	43.13	44.36	45.41
apoptosis (%)	1.32	1.53	3.44	11.5	6.35	7.47	16.8	6.76	7.94	18.3	7.14	10.40	20.1

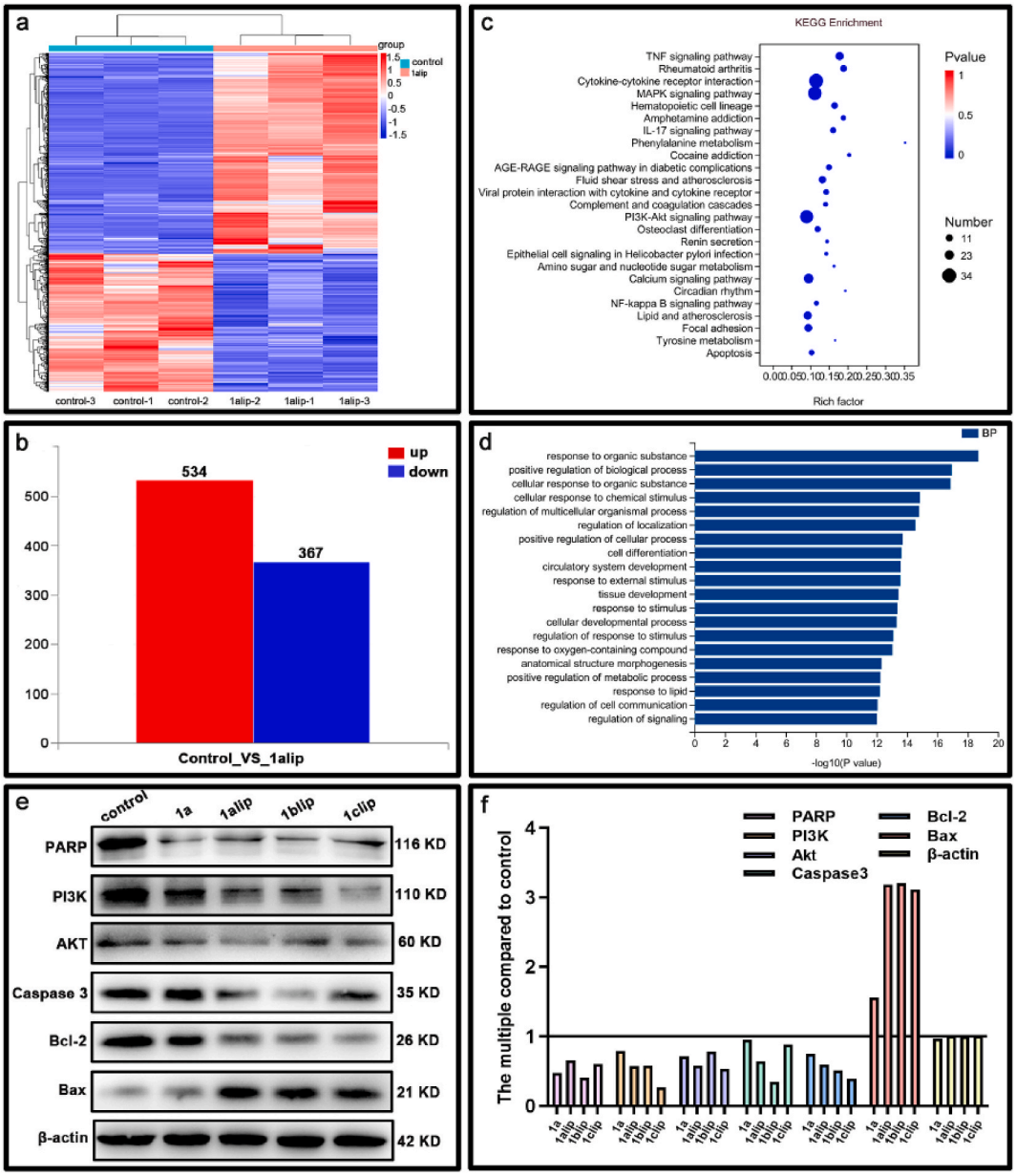

Fig. 1. RNA-sequencing assay of 1alip, (a) heatmap, (b) number of up or down-regulated genes, (c) KEGG Enrichment, (d) GO Enrichment, (e) expression of apoptosis-related proteins after a treatment of 24 h of A549 cells with 2 × IC_{50} concentration of 1alip, (f) gray values.

across the treatment groups encompassing 1a, 1alip, 1blip, and 1clip. The interplay of these molecular expressions substantiates the inference that 1a, 1alip, 1blip, and 1clip stimulate ferroptosis via GPX4 down-regulation and HMGB1 upregulation.

To further elucidate the influence of 1a, 1alip, 1blip, and 1clip on ferroptosis, we examined the cell viability in the presence of ferrostatin-1 (Fer-1), a recognized antioxidant capable of inhibiting ferroptosis. Fig. 2e underscores that the presence of Fer-1 correlates with enhanced cell viability, conclusively demonstrating the potential of 1a, 1alip, 1blip, and 1clip to induce ferroptosis. In addition, we also examined the cytotoxic activity of Fer-1 (6.25 → 400 nM) towards A549 cells during 48 h and found that Fer-1 has no cytotoxicity against A549 cells.

In the realm of assessing lipid peroxidation, 4,4-difluoro-5-(4-phenyl-1,3-butadienyl)-4-bora-3a,4a-diaza-*s*-indacene-3-undecanoic acid (C11-BODIPY$^{581/591}$) emerges as a probe to determine the lipid peroxidation [55]. Fig. 2f reveals a marked decrease in red fluorescence (indicative of non-oxidized species) accompanied by a concurrent increase in green fluorescence (indicative of oxidized species) across the treatment groups encompassing 1a, 1alip, 1blip, and 1clip. Moreover, the reduction in the red/green fluorescence ratio, as depicted in Fig. 2g, further substantiates the proclivity of 1a, 1alip, 1blip, and 1clip to cause lipid peroxidation.

2.7. Pyroptosis studies

Pyroptosis, recognized as a distinct form of programmed cell death characterized by its inflammatory nature, manifests its execution contingent upon pro-inflammatory caspase 1, accompanied by the participation of other cysteine aspartame caspases, most notably caspase 3, engendering a conspicuous release of inflammatory mediators [56]. A hallmark of pyroptotic cells lies in their distinctive morphological attributes, marked by cellular enlargement and discernible balloon-like protrusions along the cell membrane [57,58]. The observations depicted in Fig. 3a illuminate these features following a 24-h exposure of A549 cells to 1a, 1alip, 1blip, 1clip. Notably, a meticulous examination reveals that 1a leads to fewer cells adopting the pyroptotic phenotype

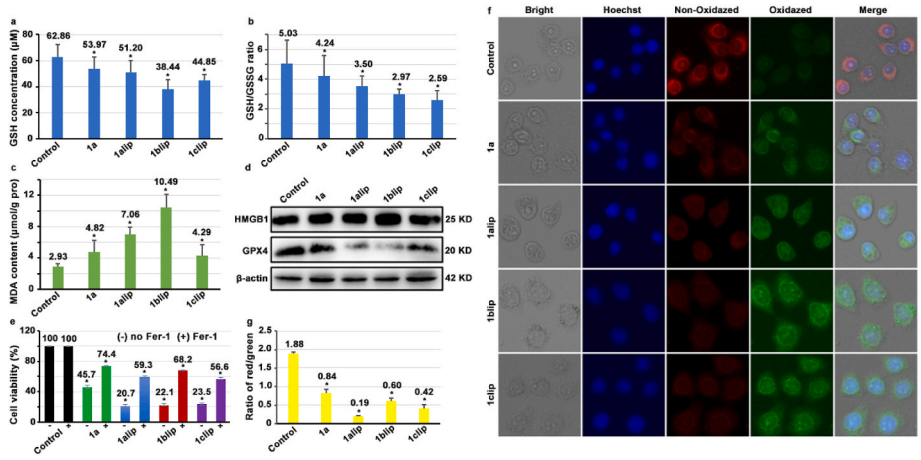

Fig. 2. (a) Intracellular GSH content, (b) ratio of GSH/GSSG, (c) MDA content, (d) expression of HMGB1 and GPX4, (e) cell viability assay in the presence Fer-1 (100 nM), (f) lipid peroxidation detection using C11-BODIPY$^{581/591}$ as a fluorescence dye, (g) ratio of red/green fluorescence, in the above assays, A549 cells were treated with IC_{50} concentration of 1a, 1alip, 1blip and 1clip for 24 h.

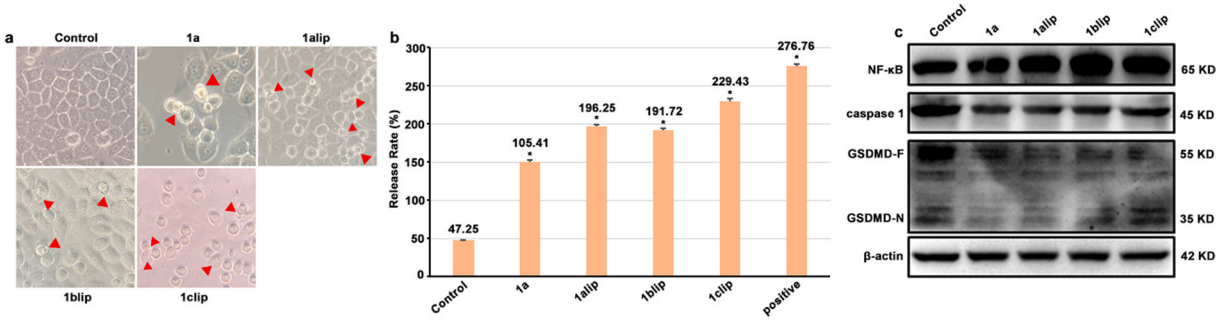

Fig. 3. Pyroptosis assay: (a) cell morphology, (b) LDH release (positive: LDH release reagent), (c) expression of NF-κB, caspase 1 and GSDME while a 24 h-treatment of A549 cells with IC_{50} concentration of 1a, 1alip, 1blip and 1clip.

when contrasted with 1alip, 1blip, and 1clip.

The lactate dehydrogenase (LDH) release assay, esteemed as a direct gauge of pyroptosis, operates on the premise of quantifying cell membrane integrity. In the assay of pyroptosis, the release of LDH from cells is emblematic of compromised cell membrane integrity, thereby resulting in an increase in LDH content [56]. The findings in Fig. 3b unmistakably illustrate an increase in LDH content, augmenting by factors of 2.23, 4.15, 4.06, and 4.86 in the groups treated with 1a, 1alip, 1blip, and 1clip, respectively. This empirical evidence underscores the pivotal role of 1a, 1alip, 1blip, and 1clip in eliciting pyroptosis.

Pyroptosis, by nature, constitutes an inflammatory cell death program that enlists the participation of NF-κB protein, wielding substantial influence over the inflammatory cascade [59]. A pivotal function of NF-κB protein resides in its orchestration of downstream protein expression, culminating in the assembly of inflammatory vesicles. This, in turn, sets in motion the activation of caspase 1, a pro-inflammatory entity, ultimately culminating in the cleavage of gasdermin D (GSDMD) proteins. The resultant cleaved N-terminal of GSDMD serves as a fulcrum, initiating perforations within the cellular membrane. The consequences encompass compromised substance exchange regulation, coupled with the emergence of vacuoles that decisively usher in the instantiation of pyroptosis [56,57,60]. Concurrently, GSDMD can also be subject to cleavage by the activated caspase 3 [25]. Fig. 3c meticulously outlines these intricate interactions, wherein the expression of NF-κB is enhanced in the 1a, 1alip, 1blip, and 1clip treatment. Converse to this, caspase 1 is demonstrably downregulated. The culminating effect materializes in the cleavage of GSDMD under the catalytic influence of activated caspase 1, engendering the generation of active N-terminal GSDMD-F. In summation, the orchestration of NF-κB activation, cascading to catalyze caspase 1 activation and GSDMD cleavage, engenders cell membrane perforation, membrane swelling, and thereby underpins the pyroptosis.

2.8. Antitumor in vivo studies

Subcutaneous injection of vigorously proliferative A549 cells into BALB/c experimental mice facilitated the development of spherical tumors. During the drug administration phase, mice were subjected to intravenous injections of 1alip at doses of 1.4 mg/kg and 2.1 mg/kg. In tandem, daily monitoring was conducted to assess body weight fluctuations and tumor dimensions. After a duration of 9 days of drug administration, the application of 1alip was terminated in both treatment cohorts. The characteristic morphology and dimensions of the tumors are expounded in Fig. 4a, revealing a substantial reduction in tumor size within the groups treated with 1.4 mg/kg and 2.1 mg/kg of 1alip compared with that in control (Fig. 4b). Notably, the tumor-suppressive efficacy of 1.4 mg/kg and 2.1 mg/kg of 1alip was quantified at 37.4 % and 70.4 %, respectively (Fig. 4c). On the 15th day, a comprehensive depiction of tumor dimensions is illustrated in Fig. 4d. This analysis evinced no significant deviations in the body weight of mice throughout the 9-day treatment period. However, a modest change in the body weight of mice within the 2.1 mg/kg 1alip group was discerned. Further insight was garnered from the assessment of relative tumor volumes, which exhibited a decline within the 1alip-treated cohort (Fig. 4e). Moreover, upon discontinuation of treatment (days 10–15), the body weights of mice exhibited no conspicuous alterations (Fig. 4f). In contrast, the relative tumor volume in the 1.4 mg/kg 1alip group exhibited a swift resurgence, approximating values observed in

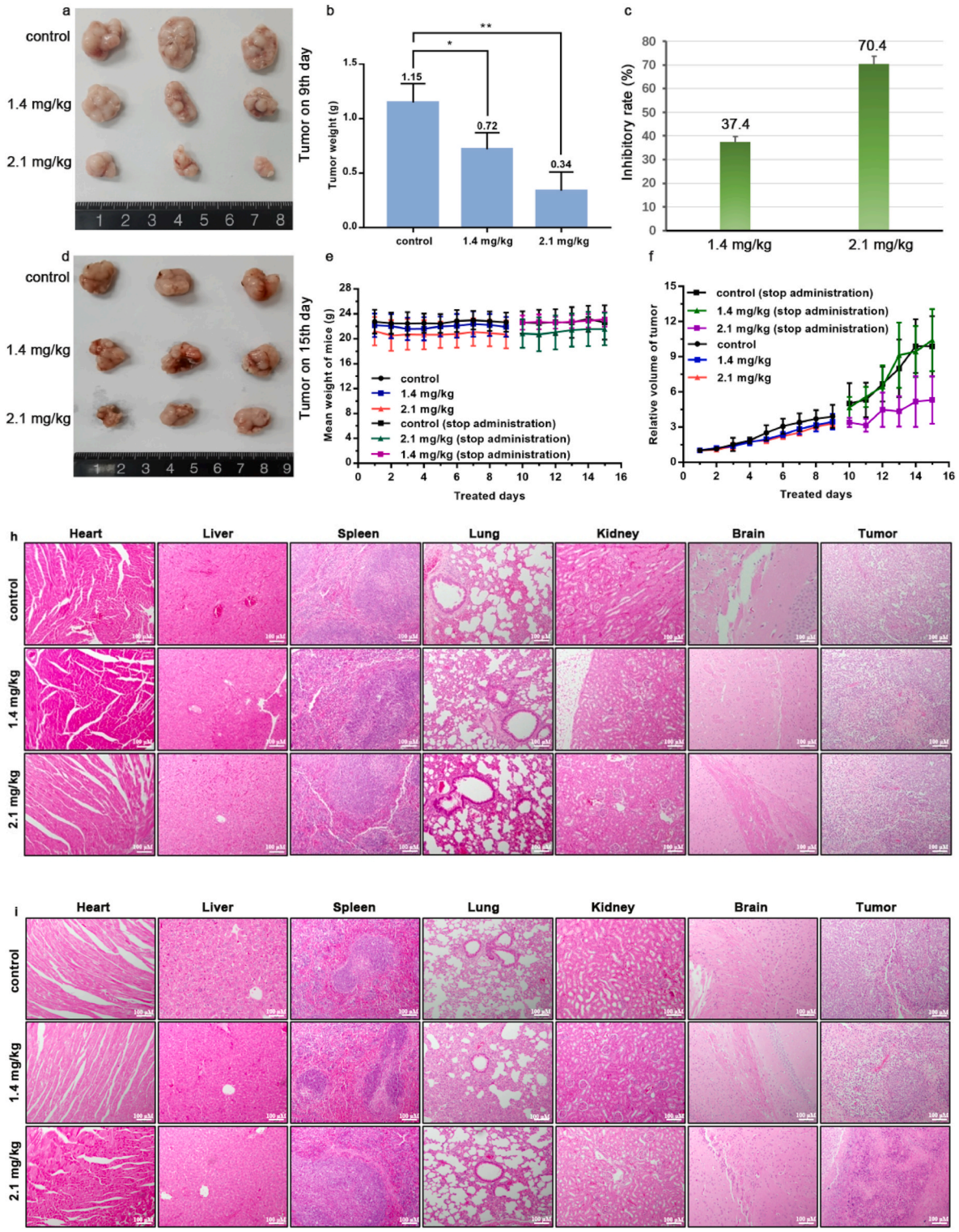

Fig. 4. (a) Tumor obtained on 9th day, (b) mean tumor weight, (c) inhibitory rate, (d) tumor obtained on 15th day, (e) mean weight of mice, (f) relative tumor volume, (h) H&E staining tissues obtained on the 9th day, (i) H&E staining tissues obtained on the 15th day.

the control group. In contrast, the relative tumor volume in the 2.1 mg/kg 1alip group exhibited marginal variation post-cessation of administration. Significantly, no instances of mortality were documented within the experimental cohort.

Detailed analysis through H&E staining (Fig. 4h) of murine tissues over the 9-day treatment interval underscored that the control group exhibited pronounced haemorrhage within the pulmonary regions, juxtaposed with comparatively minor and subdued instances of haemorrhage within the 1alip-treated groups. Tumors within the control group showed substantial mass expansion with pronounced cellular proliferation. In contrast, within the 1.4 mg/kg and 2.1 mg/kg 1alip groups, distinctive features of lamellar necrosis and a diminished tumor cell population interspersed with expansive necrotic regions were evident. Notably, no discernible deviations in the structural architecture

of the liver, brain, spleen, heart, and kidney between the control and 1alip-treated groups were observed, reaffirming no side effects associated with 1alip administration.

Upon cessation of drug administration, an analysis of H&E-stained tissues is presented in Fig. 4i. Both the control group and the two 1alip-treated cohorts exhibited pulmonary damage after drug withdrawal. Morphological scrutiny of tumor tissues in the control group exposed vigorous growth patterns, contrasted by sparse malignant cell populations within the low-concentration 1alip group, and a scarcity of malignant cells within the high-concentration 1alip group. Notably, the structural and functional integrity of the experimental groups displayed minimal variance both prior to and following the discontinuation of drug administration.

3. Conclusions

The cellular uptake reveals that 1a, 1alip, 1blip and 1clip can enter the cells, while it is difficult for 1b and 1c to enter the cells. 1a, 1alip, 1blip and 1clip locate at the mitochondria, increase the content of intracellular ROS and Ca^{2+}, reduce the mitochondrial membrane potential. The apoptosis and cell cycle distribution show that 1a, 1alip, 1blip and 1clip can cause apoptosis and inhibit A549 cell growth at the S phase. RNA-sequence studies show that 1alip downregulates the expression of 367 genes and the upregulates the expression of 534 genes and induce cell death through TNF, PI3K/AKT, and calcium ion signalling pathways. Additionally, a decrease of GSH, an increase of MDA, upregulation of HMGB1 and downregulation of GPX4, the increase of cell viability in the presence of Fer-1 and C11-BODIPY$^{581/591}$ dyed experiments suggest that 1a, 1alip, 1blip and 1clip can cause ferroptosis. The pyroptotic characteristic in the cell morphology, LDH release, the upregulation of NF-κB, downregulation of caspase 1 and the transformation from GSDMD-F to GSDMD-N indicate that 1a, 1alip, 1blip and 1clip can induce pyroptosis. Antitumor in vivo shows that 1alip can validly inhibit the tumor growth with a high inhibitory rate of 70.4 %, moreover, 1alip has no side effect on the lung, liver, kidney, heart, brain and spleen. Taken together, 1a, 1alip, 1blip and 1clip induce cell death via a ROS-mediated mitochondrial dysfunction pathway, ferroptosis and pyroptosis (Fig. 5).

4. Experimental

4.1. Materials and methods

A selection of cell lines including B16 mouse melanoma cells, A549 human lung carcinoma cells, HeLa human cervical cancer cells, HepG2 human hepatocellular carcinoma cells, HCT116 human colon cancer cells, and normal LO2 human liver cells was procured from Sun Yat-Sen University (Guangzhou). Nuclear Magnetic Resonance (NMR) spectra were meticulously recorded using a Varian-500 spectrometer operating at a frequency of 500 MHz. Dimethyl sulfoxide (DMSO-d_6) was employed as the solvent, while tetramethylsilane (TMS) served as an internal standard. High-resolution mass spectra (HRMS) were obtained through direct injection using a Waters Xevo G2-XS QTof mass analyzer.

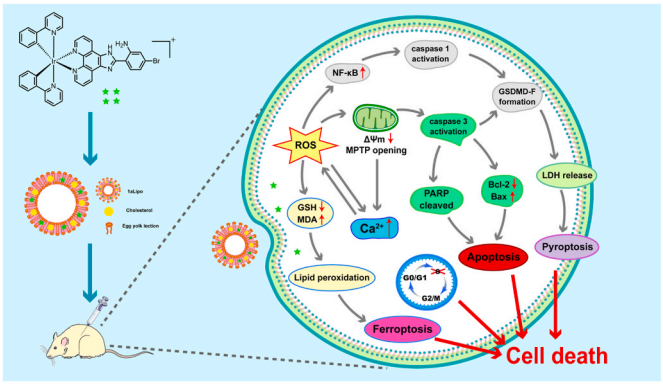

Fig. 5. Mechanism of 1alip inducing cell death in A549.

4.2. Synthesis of ligand and complexes

4.2.1. Preparation of ligand BAPIP

2-amino-4-bromobenzaldehyde (0.198 g, 1.0 mmol), 1,10-phenanthroline-5,6-dione (0.21 g, 1.0 mmol) [61], and NH_4Ac (1.54 g, 20 mmol) were meticulously placed into the flask. The mixture was dissolved in 25 mL of glacial acetic acid and refluxed for 2 h. Upon completion of the reflux, the reaction mixture was allowed to cool down. The solution was neutralized with concentrated $NH_3{\cdot}H_2O$ and the gained precipitate was thoroughly washed using ice H_2O, yielding a distinctive yellow-hued powder. Yield: 82 %. Analytical calculations for the compound $C_{19}H_{12}BrN_5$: C, 58.48 %; H, 3.10 %; N, 17.95 %. Experimental measurement values: C, 58.65 %; H, 3.23 %; N, 17.78 %. HRMS (CH_3CN): m/z = 387.4650.

4.2.2. Synthesis of [Ir(PPY$^-$)$_2$(BAPIP)](PF6) (1a)

Cis-[Ir(PPY$^-$)$_2$Cl]$_2$ (0.175 g, 0.15 mmol) [62] and BAPIP (0.117 g, 0.3 mmol) were dissolved in 15 mL of methanol and 30 mL of dichloromethane. Then the above solution was refluxed under an argon atmosphere for 6 h. After the designated reaction time, an excess of NH_4PF_6 (1 g) was introduced into the mixture and stirred for 1 h. Subsequently, the solution underwent filtration and concentration, leading to the formation of an orange-hued solid. To purify the product, crude material was subjected to neutral alumina column chromatography. The elution process employed a dichloromethane-acetone solvent mixture in a 5:1 (v/v) ratio. The orange band was collected and concentrated to yield a yellow powder, yield: 84 %. The molecular formula of the compound was identified as $C_{41}H_{28}BrF_6PN_7Ir$. ^{1}H NMR (DMSO-d_6, 500 MHz, Fig. S5a and SI): δ 8.26 (d, J = 8.5 Hz, 2H), 8.15 (dd, J = 1.5, J = 5.0 Hz, 2H), 8.10–8.07 (m, 2H), 7.96 (d, J = 8.0 Hz, 4H), 7.88 (t, J = 7.5 Hz, 2H), 7.51 (d, J = 5.5 Hz, 2H), 7.16 (d, J = 7.0 Hz, 1H), 7.07 (t, J = 7.0, 2H), 7.00–6.93 (m, 6H), 6.30 (d, J = 7.5 Hz, 2H), 4.49 (s, 2H). ^{13}C NMR (DMSO-d_6, 125 MHz, Fig. 5b and SI): 167.38, 153.72, 153.37, 150.85, 149.87, 149.63, 148.83, 144.51, 139.17, 132.93, 131.70, 130.74, 129.63, 127.46, 126.03, 125.55, 124.69, 124.31, 122.85, 120.45, 118.71, 118.19. HRMS (CH_3CN): m/z = 890.1215 ([M − PF_6]$^+$).

4.2.3. Synthesis of [Ir(PIQ$^-$)$_2$(BAPIP)] (PF6) (1b)

Synthesis of [Ir(PIQ$^-$)$_2$(BAPIP)](PF_6) (1b) is closely similar to 1a. In this case, the starting material *cis*-[Ir(PIQ$^-$)$_2$Cl]$_2$ [62] replaced *cis*-[Ir(PPY$^-$)$_2$Cl]$_2$, yield: 80 %. Molecular formula: $C_{49}H_{32}BrF_6PN_7Ir$. ^{1}H NMR (DMSO-d_6, 500 MHz, Fig. S6a and SI): δ 9.09 (d, J = 9.0 Hz, 2H), 9.02 (d, J = 8.0, 2H), 8.40 (d, J = 8.0 Hz, 2H), 8.01–7.99 (m, 2H), 7.90–7.84 (m, 9H), 7.44 (d, J = 6.5 Hz, 2H), 7.37 (d, J = 6.5 Hz, 2H), 7.17 (t, J = 7.0 Hz, 2H), 7.01–6.96 (m, 4H), 6.31 (d, J = 7.5 Hz, 2H). ^{13}C NMR (DMSO-d_6, 125 MHz, Fig. S6b and SI): 172.52, 168.31, 155.21, 154.39, 153.74, 146.81, 145.82, 144.16, 141.24, 136.96, 132.92, 132.50, 132.16, 131.10, 131.02, 129.85, 129.70, 128.16, 127.32, 126.91, 126.01, 122.80, 122.66, 121.57, 118.57, 118.10. HRMS (CH_3CN): m/z = 990.1518 ([M − PF_6]$^+$).

4.2.4. Synthesis of [Ir(BZQ$^-$)$_2$(BAPIP)] (PF6) (1c)

The synthesis procedure for [Ir(BZQ$^-$)$_2$(BAPIP)] (PF_6) (1c) paralleled that of 1a, with the substitution of *cis*-[Ir(PPY$^-$)$_2$Cl]$_2$ with *cis*-[Ir(BZQ$^-$)$_2$Cl]$_2$ [62], yield: 78 %. Molecular formula: $C_{45}H_{28}BrF_6PN_7Ir$. ^{1}H NMR (DMSO-d_6, 500 MHz, Fig. S7a and SI): δ 9.29 (d, J = 8.0 Hz, 2H), 8.53 (dd, J = 1.0, J = 5.0 Hz, 2H), 8.13 (d, J = 4.5 Hz, 2H), 8.04–7.94 (m, 7H), 7.92–7.88 (m, 2H), 7.60 (d, J = 7.0 Hz, 2H), 7.45 (q, 2H), 7.24 (t, J = 7.0 Hz, 2H), 7.15 (d, J = 2.0 Hz, 1H), 6.93 (dd, J = 2.0, J = 8.5 Hz, 1H), 6.33 (d, J = 7.0 Hz, 2H), 4.48 (s, 2H). ^{13}C NMR (DMSO-d_6, 125 MHz, Fig. 7b and SI): 158.44, 154.89, 151.41, 150.89, 149.19, 146.48,

142.38, 139.57, 135.78, 134.57, 131.76, 131.52, 131.12, 130.57, 129.05, 128.73, 126.24, 124.77, 122.38, 120.23, 119.73. HRMS (CH_3CN): $m/z = 938.1209$ ($[M - PF_6]^+$).

4.3. Preparation of 1alip, 1blip and 1clip

Liposomes were prepared based on the thin film hydration technique [63]. A mixture of PC-98T 30 mg, CHO-HP 6 mg, DSPE-mPEG2000 5 mg and iridium(III) complex 1 mg was dissolved in 6 mL ethanol/chloroform (1:2, v/v). The mixture was then transferred to a pear-shaped flask. The organic reagent was dried in a 328 K water bath using a rotary vacuum evaporator and wholly removed under vacuum for 3 h. In 328 K water bath, 5 mL phosphate-buffered saline (PBS) was used to hydrate the dried lipid membrane. In addition, the liposome suspension was ultrasonically treated with a 150W ultrasonic cell grinder for 6 min. Then the liposome was centrifuged at 11000 rpm for 10 min. Finally, the supernatant was collected as liposomes and stored in 277 K refrigerators.

Note: The experimental procedures for determination of encapsulation efficiency, liposome size and zeta potential, drug release, cell culture, cellular uptake, mitochondrial localization, mitochondrial membrane potential, mitochondrial permeability transition pore, intracellular ROS, Ca^{2+} levels, RNA sequencing analysis, glutathione (GSH) and malondialdehyde (MDA) measurement can be found in the supplementary materials.

4.4. In vitro cytotoxicity assessment

To evaluate the cytotoxic potential of 1a, 1b, 1c, 1alip, 1blip, and 1clip, a widely employed 3-(4,5-dimethylthiazol-2-yl)-2,5-diphenyltetrazolium bromide (MTT) assay [34] was conducted. Cancer cell lines were seeded into 96-well microarray plates at a density of 1×10^4 cells per well. A range of distinct concentrations of the complexes were added to the plates. Following 48 h of incubation, a fresh serum-free medium-MTT (9:1, v/v) solution was added to each well. The cells were subsequently incubated at 37 °C for an additional 4 h. Finally, Dimethyl sulfoxide was applied to dissolve MTT followed by measurement of the absorbance at 490 nm.

4.5. Cell cycle arrest studies

A549 cells were seeded in a 6-well plate at a density of 5×10^5 cells per well and allowed to adhere overnight. Subsequently, the cells were treated with 1a, 1alip, 1blip, and 1clip for a duration of 24 h. Following treatment, the cells were collected through trypsinization, then rinsed with cold PBS, and finally fixed with 70 % ethanol overnight. The next steps involved the addition of 0.1 % Triton X-100, 20 μL of RNAse (0.2 mg/mL), and 20 μL of PI (propidium iodide) solution (0.02 mg/mL) to the cell suspensions. This mixture was incubated at 37 °C for 30 min, after which the cells were analyzed utilizing FACSCalibur flow cytometry.

4.6. Apoptosis assay using Annexin V-FITC/PI staining

A549 cells were cultured into a 6-well plate overnight, the cells were exposed to 1a, 1alip, 1blip, and 1clip for a duration of 24 h. Post-treatment, the cells were detached through trypsinization, followed by staining using the Annexin V-FITC/PI Assay Kit. Flow cytometry analysis (Beckman Instruments, NJ) was then employed to evaluate the stained cells.

4.7. Western blotting analysis

Following treatment with 1a, 1alip, 1blip, and 1clip, exponentially growing A549 cells underwent a series of methodical steps. The cells were initially washed with cold PBS and subsequently lysed using lysis buffer. The resulting lysate was then centrifuged at 12,000 g for a duration of 20 min. Determination of protein concentration within the supernatant was accomplished using the BCA kit (Beyotime Biotech, Shanghai, China). Equal quantities of proteins were subjected to fractionation through SDS-polyacrylamide gel electrophoresis (SDS-PAGE). Subsequently, the proteins were transferred to polyvinylidene difluoride (PVDF) membranes (Millipore, MA, USA), which were subsequently blocked using a 5 % non-fat milk solution in TBST (20 mM Tris-HCl, 150 mM NaCl, 0.05 % Tween 20, pH 8.0) buffer for a duration of 1 h. The membranes were then subjected to an overnight hybridization with primary antibodies. This was followed by an additional incubation with an appropriate secondary antibody conjugated with horseradish peroxidase. Finally, the protein expression levels were visualized utilizing a chemiluminescence (ECL) detection kit.

4.8. Intracellular lipid peroxidation

A549 cells were seeded in a 6-well plate overnight. Then the cells were incubated with 1a, 1alip, 1blip and 1clip for a period of 24 h. Post-treatment, the cells underwent triple washing with PBS and were then stained with BODIPY-C11 581/591 (2.5 μM) for 30 min at 37 °C. The subsequent imaging of cells was gained under a fluorescence microscope, while the determination of fluorescence intensity was conducted using flow cytometry.

4.9. Ferrostatin-1 (Fer-1) assay

In the Fer-1 assay, A549 cells were initially cultured in a 96-well plate for a duration of 24 h. The cells within the 96-well microarray plate were subsequently divided into distinct groups, including control, control + Fer-1, 1a, 1a + Fer-1, 1alip, 1alip + Fer-1, 1b, 1blip + Fer-1, 1cip, and 1clip + Fer-1. Following a 24-h interval, the cells were treated with MTT for 4 h. Eventually, 100 μL dimethyl sulfoxide was introduced to dissolve the residual MTT, determining the absorbance at 490 nm.

4.10. Cell morphology and lactate dehydrogenase release

In the pursuit of cell morphology and lactate dehydrogenase (LDH) release investigations, A549 cells were initially seeded in a 6-well plate. This was followed by an overnight incubation at 37 °C. The cells were then treated with 1a, 1alip, 1blip, and 1clip for 24 h. Afterwards, the cell morphology was meticulously observed under an inverted light microscope.

For LDH release studies, cells cultured in a 96-well plate were co-incubated with 1a, 1alip, 1blip, and 1clip for a period of 24 h. Following this treatment, the control groups were exposed to an LDH-release solution for an hour. Thereafter, the supernatant from all wells was transferred to new wells and mixed with LDH detection working solution at 25 °C for 30 min, with precautions taken to avoid light. The absorbance was measured at 490 nm.

4.11. In vivo anti-tumor experiment

Given the evident toxicity of 1alip to A549 cells *in vitro*, the in vivo antitumor efficiency of 1alip was investigated using an A549 xenografts model. Experimental mice were provided by Guangdong Medical Laboratory Animal Center (Guangzhou, China). All experimental procedures abided by the rules and regulations drawn up by the Animal Ethics Committee of Guangdong Pharmaceutical University. The cells were cultivated in a thermostatic incubator at 37 °C under 5 % CO_2 and 100 % humidity. The mice were randomized into three groups ($n = 6$). To establish the tumor model, A549 cells were subcutaneously injected into the flank of each mouse. Post 7 days, intraperitoneal (i.p.) administration of 1alip (2.1 mg/kg and 1.4 mg/kg) was initiated, spanning from days 1–9. The control group received injections of normal saline exclusively. The tumor size and the mice's weights were measured and

recorded daily. Upon completion of the administration period, half of the mice from each group were euthanized, while the remaining mice were observed daily, and the tumor size and body weight of mice were recorded. The lung, heart, liver, brain, and spleen were collected.

4.12. Data analysis

Data were presented as mean ± SD. Statistical treatment was performed using a *t*-test. Differences were considered significant at $^{*}p < 0.05$.

CRediT authorship contribution statement

Chunxia Huang: Writing – original draft, Methodology, Investigation. **Yuhan Yuan:** Methodology, Investigation. **Gechang Li:** Formal analysis, Data curation. **Shuang Tian:** Formal analysis, Data curation. **Huiyan Hu:** Software. **Jing Chen:** Data curation. **Lijuan Liang:** Formal analysis. **Yi Wang:** Software. **Yunjun Liu:** Writing – review & editing, Supervision, Project administration, Funding acquisition, Conceptualization.

Declaration of competing interest

Authors declare no competing interests exist.

Data availability

Data will be made available on request.

Acknowledgements

We are grateful to the National Nature Science Foundation of China (No 21877018).

Appendix A. Supplementary data

Supplementary data to this article can be found online at https://doi.org/10.1016/j.ejmech.2023.116112.

References

[1] B.R. Tian, Y.M. Liu, J.Y. Liu, Cyclodextrin as a magic switch in covalent and non-covalent anticancer drug release systems, Carbohyd, Polym 242 (2020) 116401.
[2] R.S. Riley, C.H. June, R. Langer, M.J. Mitchell, Delivery technologies for cancer immunotherapy, Nat. Rev. Drug Discov. 18 (2019) 175–196.
[3] X.M. Anguela, K.A. High, Entering the modern Era of gene therapy, Annu. Rev. Med. 70 (2019) 273–288.
[4] M. Davern, J. Lysaght, Cooperation between chemotherapy and immunotherapy in gastroesophageal cancers, Cancer Lett. 495 (2020) 89–99.
[5] P. Chellan, P.J. Sadler, Enhancing the activity of drugs by conjugation to organometallic fragments, Chem. Eur J. 26 (2020) 8676–8688.
[6] M.A. Farooq, M. Aquib, A. Farooq, D. Haleem Khan, M.B. Joelle Maviah, M. Sied Filli, S. Kesse, K.O. Boakye-Yiadom, R. Mavlyanova, A. Parveen, B. Wang, Recent progress in nanotechnology-based novel drug delivery systems in designing of cisplatin for cancer therapy: an overview, Artificial cells, nanomedicine, and biotechnology 47 (2019) 1674–1692.
[7] P.C. Bruijnincx, P.J. Sadler, New trends for metal complexes with anticancer activity, Curr. Opin. Chem. Biol. 12 (2008) 197–206.
[8] R.R. Ye, J.J. Cao, C.P. Tan, L.N. Ji, Z.W. Mao, Valproic acid-functionalized cyclometalated iridium(III) complexes as mitochondria-targeting anticancer agents, Chem. Eur J. 23 (2017) 15166–15176.
[9] A. Petrini, R. Pettinari, F. Marchetti, C. Pettinari, B. Therrien, A. Galindo, R. Scopelliti, T. Riedel, P.J. Dyson, Cytotoxic half-sandwich Rh(III) and Ir(III) β-diketonates, Inorg. Chem. 56 (2017) 13600–13612.
[10] L. Liu, J. Chen, M.M. Wang, Y.L. Huang, Y. Qian, X.L. Xue, Z. Su, H.K. Liu, The cyclometalated iridium (III) complex based on 9-anthracenecarboxylic acid as a lysosomal-targeted anticancer agent, J. Inorg. Biochem. 235 (2022) 111913.
[11] S.J. Wu, S.G. Wang, Z.B. Li, C. Wu, D.L. Ma, X.M. Miao, G-quadruplex-selective iridium(III) complex as a novel electrochemiluminescence probe for switch-on assay of double-stranded DNA, Anal. Bioanal. Chem. 414 (2022) 3755–3763.
[12] L.J. Liang, Y. Yang, H.M. Liu, F. Yuan, Y.H. Yuan, W.L. Li, C.X. Huang, J. Chen, Y. J. Liu, Anticancer efficacy evaluation of ruthenium(II) and iridium(III) polypyridyl complexes toward A549 cells, J. Biol. Inorg. Chem. 28 (2023) 421–437.
[13] X.C. Liu, Z. Wang, X.R. Zhang, X.C. Lv, Y. Song, R.X. Dong, G.X. Li, X.Y. Ren, Z. Y. Ji, X.A. Yuan, Z. Liu, Configurationally regulated half-sandwich iridium(III)-ferrocene heteronuclear metal complexes: potential anticancer agents, J. Inorg. Biochem. 249 (2023) 112393.
[14] S.Y. Guo, F.M. Wei, J. Karges, Y.K. Zhao, L.N. Ji, H. Chao, Cancer cell membrane-camouflaged and h2o2-activatable nanocomposites for synergistic chemotherapy and two-photon photodynamic therapy against melanoma, Inorg. Chem. Front. 10 (2023) 2716–2730.
[15] J. Chen, H.M. Liu, Y.C. Chen, H.Y. Hu, C.X. Huang, Y. Wang, L.J. Liang, Y.J. Liu, Iridium(III) complexes inhibit the proliferation and migration of bel-7402 cells through the pi3k/akt/mtor signaling pathway, J. Inorg. Biochem. 241 (2023) 112145.
[16] J. Bonelli, E. Ortega-Forte, G. Vigueras, M. Bosch, N. Cutillas, J. Rocas, J. Ruiz, V. Marchán, Polyurethane-polyurea hybrid nanocapsules as efficient delivery systems of anticancer Ir(III) metallodrugs, Inorg. Chem. Front. 9 (2022) 2123–2138.
[17] Y.H. Yuan, Y.Y. Zhang, J. Chen, C.X. Huang, H.M. Liu, W.L. Li, L.J. Liang, Y. Wang, Y.J. Liu, Synthesis, biological evaluation of novel iridium(III) complexes targeting mitochondria toward melanoma b16 cells, Eur. J. Med. Chem. 247 (2023) 115046.
[18] A.R. Rubio, J. Fidalgo, J. Martin-Vargas, C. Pérez-Arnaiz, S.R. Alonso-Torre, T. Biver, G. Espino, N. Busto, B. García, Biological activity and photocatalytic properties of a naphthyl-imidazo phenanthroline (HNAIP) ligand and its [Ir $(ppy)_2$(HNAIP)]Cl and [Rh$(ppy)_2$(HNAIP)]Cl complexes, J. Inorg. Biochem. 203 (2020) 110885.
[19] Y. Shi, R. van der Meel, X.Y. Chen, T. Lammers, The EPR effect and beyond: strategies to improve tumor targeting and cancer nanomedicine treatment efficacy, Theranostics 10 (2020) 7921–7924.
[20] T. Yang, B. Li, S.B. Qi, Y. Liu, Y.K. Gai, P. Ye, G. Yang, W.D. Zhang, P. Zhang, X. X. He, W.J. Li, Z.P. Zhang, G.Y. Xiang, C.R. Xu, Co-delivery of doxorubicin and Bmi1 siRNA by folate receptor targeted liposomes exhibits enhanced anti-tumor effects in vitro and in vivo, Theranostics 4 (2014) 1096–1111.
[21] G. Yang, T. Yang, W.D. Zhang, M. Lu, X. Ma, G.Y. Xiang, In Vitro and in vivo antitumor effects of folate-targeted ursolic acid stealth liposome, J. Age Food Chem. 62 (2014) 2207–2215.
[22] W.C. Zamboni, Liposomal, nanoparticle, and conjugated formulations of anticancer agents, Clin. Cancer Res. 11 (2005) 8230–8234.
[23] B. Almeida, O.K. Nag, K.E. Rogers, J.B. Delehanty, Recent progress in bioconjugation strategies for liposome-mediated drug delivery, Molecules 25 (2020) 5672.
[24] B.Y. Yang, B.P. Song, S.N. Shankar, A. Guller, W. Deng, Recent advances in liposome formulations for breast cancer therapeutics, Cell. Mol. Life Sci. 78 (2021) 5225–5243.
[25] H.W. Zhang, X.F. Liao, X.Y. Wu, C.L. Shi, Y.Y. Zhang, Y.H. Yuan, W.L. Li, J. W. Wang, Y.J. Liu, Iridium(III) complexes entrapped in liposomes trigger mitochondria-mediated apoptosis and GSDME-mediated pyroptosis, J. Inorg. Biochem. 228 (2022) 111706.
[26] Y.Y. Zhang, W.D. Fei, H.W. Zhang, Y. Zhou, L. Tian, J. Hao, Y.Y. Yuan, W.L. Li, Y. J. Liu, Increasing anticancer effect in vitro and vivo of liposome-encapsulated iridium(III) complexes on BEL-7402 cells, J. Inorg. Biochem. 225 (2021) 111622.
[27] Y.C. Chen, Y.Y. Gu, H.Y. Hui, H.M. Liu, W.L. Li, C.X. Huang, J. Chen, L.J. Liang, Y. J. Liu, Design, synthesis and biological evaluation of liposome entrapped iridium (III) complexes toward SGC-7901 cells, J. Inorg. Biochem. 241 (2023) 112134.
[28] Y.Y. Zhang, H.W. Zhang, L. Tian, J. Hao, Y.H. Yuan, W.L. Li, Y.J. Liu, DNA-binding and evaluation of anticancer activity in vitro and in vivo of iridium(III) polypyridyl complexes, J. Inorg. Biochem. 224 (2021) 111580.
[29] Y. Zhou, L. Bai, L. Tian, L.L. Yang, H.W. Zhang, Y.Y. Zhang, J. Hao, Y.Y. Gu, Y. J. Liu, Iridium(III)-BBIP Complexes Induce Apoptosis via PI3K/AKT/mTOR Pathway and Inhibit A549 Lung Tumor Growth in Vivo, vol. 223, 2021 111550.
[30] J. Staroń, W. Pietruś, R. Bugno, R. Kurczab, G. Satała, D. Warszycki, T. Lenda, A. Wantuch, A.S. Hogendorf, A. Hogendorf, B. Duszyńska, A.J. Bojarski, Tuning the activity of known drugs via the introduction of halogen atoms, a case study of SERT ligands – Fluoxetine and fluvoxamine, Eur. J. Med. Chem. 220 (2021) 113533.
[31] D.Q. Song, N.N. Du, Y.M. Wang, W.Y. He, E.Z. Zhang, S.X. Cheng, Y.X. Wang, Y. H. Li, Y.P. Wang, X. Li, J.D. Jiang, Synthesis and activity evaluation of phenylurea derivatives as potent antitumor agents, Bioorg. Med. Chem. 17 (2009) 3973, 3878.
[32] T.A. Dias, C.L. Duarte, C.F. Lima, M.F. Proença, C. Pereira-Wilson, Superior anticancer activity of halogenated chalcones and flavonols over the natural flavonol quercetin, Eur. J. Med. Chem. 65 (2013) 500–510.
[33] Y. Ichimaru, T. Fujii, H. Saito, M. Sano, T. Uchiyama, S. Miyairi, 5-Bromoindirubin 30-(O-oxiran-2-ylmethyl)oxime: a long-acting anticancer agent and a suicide inhibitor for epoxide hydrolase, Bioorg. Med. Chem. 25 (2017) 4665–4676.
[34] T. Mosmann, Rapid colorimetric assay for cellular growth and survival: application to proliferation and cytotoxicity assays, J. Immunol. Methods 65 (1983) 55–63.
[35] L. Bai, W.D. Fei, Y.Y. Gu, M. He, F. Du, L.L. Yang, Y.J. Liu, Liposomes encapsulated iridium(III) polypyridyl complexes enhance anticancer activity in vitro and in vivo, J. Inorg. Biochem. 205 (2020) 111014.
[36] E. Seppet, M. Gruno, A. Peetsalu, Z. Gizatullina, H.P. Nguyen, S. Vielhaber, M. Wussling, S. Trumbeckaite, O. Arandarcikaite, D. Jerzembeck, M. Sonnabend, K. Jegorov, S. Zierz, F. Striggow, F.N. Gellerich, Mitochondria and energetic depression in cell pathophysiology, Int. J. Mol. Sci. 10 (2009) 2252–2303.
[37] C.F. Huang, C. Freter, Lipid metabolism, apoptosis and cancer therapy, Int. J. Mol. Sci. 16 (2015) 924–949.
[38] K. Elefantova, B. Lakatos, J. Kubickova, Z. Sulova, A. Breier, Detection of the mitochondrial membrane potential by the cationic dye JC-1 in L1210 cells with massive overexpression of the plasma membrane ABCB1 drug transporter, Int. J. Mol. Sci. 19 (2018) 1985.

[39] S.J. Ralph, R. Pritchard, S. Rodriguez-Enriquez, R. Moreno-Sanchez, R.K. Ralph, Hitting the Bull's-Eye in Metastatic cancers-NSAIDs elevate ROS in mitochondria, inducing malignant cell death, Pharmaceuticals 8 (2015) 62–106.
[40] Y.Y. Wei, H.N. Sun, B. Yan, Oxidized Graphene Alleviates benzo[α]pyrene-induced cytotoxicity by suppressing mitochondrial apoptosis pathways, Acs. Sustain Chem. Eng. 11 (2023) 1917–1927.
[41] C.C. Cui, R. Merritt, L.W. Fu, Z. Pan, Targeting calcium signaling in cancer therapy, Acta Pharm. Sin. B 7 (2017) 3–17.
[42] E. Bertero, C. Maack, Calcium signaling and reactive oxygen species in mitochondria, Circ. Res. 122 (2018) 1460–1478.
[43] S. Diaz-Moralli, M. Tarrado-Castellarnau, A. Miranda, M. Cascante, Targeting cell cycle regulation in cancer therapy, Pharmacology Therapeut 138 (2013) 255–271.
[44] R.M. Mohammad, I. Muqbil, L. Lowe, C. Yedjou, H. Hsu, L. Lin, M.D. Siegelin, C. Fimognari, N.B. Kumar, Q.P. Dou, H. Yang, A.K. Samadi, G.L. Russo, C. Spagnuolo, S.K. Ray, M. Chakrabarti, J.D. Morre, H.M. Coley, K. Honoki, H. Fujii, A.G. Georgakilas, A. Amedei, E. Niccolai, A. Amin, S.S. Ashraf, W. G. Helferich, X. Yang, C.S. Boosani, G. Guha, D. Bhakta, M.R. Ciriolo, K. Aquilano, S. Chen, S.I. Mohammed, W.N. Keith, A. Bilsland, D. Halicka, S. Nowsheen, A. S. Azmi, Broad targeting of resistance to apoptosis in cancer, Semin. Cancer Biol. 35 (2015) S78–S103.
[45] S. Zaman, R. Wang, V. Gandhi, Targeting the apoptosis pathway in hematologic malignancies, Leuk. Lymphoma 55 (2014) 1980–1992.
[46] C. Pfeffer, A. Singh, Apoptosis: a target for anticancer therapy, Int. J. Mol. Sci. 19 (2018) 448.
[47] E. Bankell, S. Dahl, O. Gidlof, D. Svensson, B.O. Nilsson, LL-37-induced caspase-independent apoptosis is associated with plasma membrane permeabilization in human osteoblast-like cells, Peptides 135 (2021) 170432.
[48] M.M. Gaschler, B.R. Stockwell, Lipid peroxidation in cell death, Biochem. Bioph. Res. Co. 482 (2017) 419–425.
[49] S.C. Lu, Regulation of glutathione synthesis, Mol. Aspects Med 30 (2009) 42–59.
[50] R.J. He, M. Cui, H. Lin, L. Zhao, J.Y. Wang, S.F. Chen, Z.W. Shao, Melatonin resists oxidative stress-induced apoptosis in nucleus pulposus cells, Life Sci. 199 (2018) 122–130.
[51] Y. Su, B. Zhao, L. Zhou, Z. Zhang, Y. Shen, H. Lv, L.H.H. AlQudsy, P. Shang, Ferroptosis, a novel pharmacological mechanism of anti-cancer drugs, Cancer Lett. 483 (2020) 127–136.
[52] W.S. Yang, R. SriRamaratnam, M.E. Welsch, K. Shimada, R. Skouta, V. S. Viswanathan, J.H. Cheah, P.A. Clemons, A.F. Shamji, C.B. Clish, L.M. Brown, A. W. Girotti, V.W. Cornish, S.L. Schreiber, B.R. Stockwell, Regulation of Ferroptotic cancer cell death by GPX4, Cell 156 (2014) 317–331.
[53] D.F. Zhang, C.L. Wu, D.Y. Ba, N. Wang, Y.L. Wang, X.L. Li, Q.Y. Li, G.F. Zhao, Ferroptosis contribute to neonicotinoid imidacloprid-evoked pyroptosis by activating the HMGB1-RAGE/TLR4-NF-κB signaling pathway, Ecotoxicol. Environ. Saf. 253 (2023) 114655.
[54] K.Y. Zhu, X. Zhu, S.Q. Liu, J. Yu, S.W. Wu, M.Y. Hei, Glycyrrhizin Attenuates Hypoxic-Ischemic brain damage by inhibiting ferroptosis and Neuroinflammation in Neonatal Rats via the HMGB1/GPX4 pathway, Oxid. Med. Cell. Longev. (2022) 8438528.
[55] G.P. Drummen, L.C. van Liebergen, J.A. Op den Kamp, J.A. Post, C11-BODIPY$^{(581/591)}$, an oxidation-sensitive fluorescent lipid peroxidation probe: (micro) spectroscopic characterization and validation of methodology, Free Radic. Biol. Med. 33 (2002) 473–490.
[56] L. Galluzzi, I. Vitale, S.A. Aaronson, J.M. Abrams, D. Adam, P. Agostinis, E. S. Alnemri, L. Altucci, I. Amelio, D.W. Andrews, M. Annicchiarico-Petruzzelli, A. V. Antonov, E. Arama, E.H. Baehrecke, N.A. Barlev, N.G. Bazan, F. Bernassola, M.J. M. Bertrand, K. Bianchi, M.V. Blagosklonny, K. Blomgren, C. Borner, P. Boya, C. Brenner, M. Campanella, Molecular mechanisms of cell death: recommendations of the Nomenclature Committee on cell death 2018, Cell Death Differ. 25 (2018) 486–541.
[57] D. Chen, S.W. Guo, X.G. Tang, Y. Rong, H.B. Bo, H. Shen, Z.Z. Zhao, A.M. Qiao, J. Shen, J.Q. Wang, Combination of ruthenium (II) polypyridyl complex Δ-Ru1 and Taxol enhances the anti-cancer effect on Taxol-resistant cancer cells through Caspase-1/GSDMD-mediated pyroptosis, J. Inorg. Biochem. 230 (2022) 111749.
[58] J.J. Ding, K. Wang, W. Liu, Y. She, Q. Sun, J.J. Shi, H.Z. Sun, D.C. Wang, F. Shao, Pore-forming activity and structural autoinhibition of the gasdermin family, Nature 535 (2016) 111–116.
[59] X. Dolcet, D. Llobet, J. Pallares, X. Matias-Guiu, NF-kB in development and progression of human cancer, Virchows Arch. 446 (2005) 475–482.
[60] B.T. Cookson, M.A. Brennan, Pro-inflammatory programmed cell death, Trends Microbiol. 9 (2001) 113–114.
[61] W. Paw, R. Eisenberg, Synthesis, characterization, and spectroscopy of dipyridocatecholate complexes of platinum, Inorg. Chem. 36 (1997) 2287–2293.
[62] S. Sprouse, K.A. King, P.J. Spellane, R.J. Watts, Photophysical effects of metal-carbon sigma bonds in ortho-metalated complexes of iridium(III) and rhodium(III), J. Am. Chem. Soc. 106 (1984) 6647–6653.
[63] S.L. Huang, R.C. MacDonald, Acoustically active liposomes for drug encapsulation and ultrasound-triggered release, Biochim. Biophys. Acta 1665 (2004) 134–141.